Combustion and Flame 213 (2020) 291–301

Contents lists available at ScienceDirect

Combustion and Flame

journal homepage: www.elsevier.com/locate/combustflame

OH^* chemiluminescence in the H_2–NO_2 and H_2–N_2O systems

Clayton R. Mulvihill*, Eric L. Petersen

J. Mike Walker '66 Department of Mechanical Engineering, Texas A&M University, College Station, TX 77843, USA

ARTICLE INFO

Article history:
Received 3 April 2019
Revised 2 June 2019
Accepted 13 November 2019

Keywords:
Shock tubes
Emission
Hydrogen
Nitrogen dioxide
Nitrous oxide

ABSTRACT

Shock-tube experiments were performed in a mixture of 0.222% H_2/0.392% NO_2/Ar between 1535 and 2003 K near 1.1 atm. Time histories of OH^* chemiluminescence from the $A \rightarrow X$ band near 307 nm were recorded and showed poor agreement with predictions from a recent hydrocarbon/NO_x model when only the OH^*-forming reactions $N_2O + H \leftrightarrows N_2 + OH^*$ (R2) and $O + H (+M) \leftrightarrows OH^* (+M)$ (R3) were included. Since chemiluminescence is strongly correlated with heat release and since the reaction $NO_2 + H \leftrightarrows NO+OH$ is known to be primarily responsible for heat release during H_2–NO_2 oxidation, the chemiluminescent reaction

$$NO_2 + H \leftrightarrows NO + OH^* \quad (R1)$$

was proposed for the first time. By fitting the experimental OH^* data, a best-fit rate constant was obtained as $k_1 = 7.0 \times 10^{13} \exp(-27,680/T)$, with k_1 in $cm^3\ mol^{-1}\ s^{-1}$ and T in K. This expression for k_1 is valid in the experimental temperature range of 1535 to 2003 K. The fitted k_1 value is dependent on the base NOx mechanism used. OH^* profiles were also acquired in a mixture of 0.333% H_2/0.666% N_2O/Ar between 1448 and 1776 K near 1.1 atm. The introduction of the new reaction R1 into the mechanism had no effect on the modeling of either the newly acquired H_2–N_2O OH^* data or previous H_2–N_2O OH^* data from the literature. Finally, R1 and R2 violate a long-held assumption concerning the exothermicity of such reactions, suggesting that the exothermicity criteria used to evaluate potential chemiluminescent reactions could be relaxed in future studies. Instead, a new methodology based on both the enthalpy of reaction and the entropy of reaction could be employed to identify new chemiluminescent reactions. To the best of the authors' knowledge, this is the first detailed study of OH^* chemiluminescence kinetics in the H_2–NO_2 system.

1. Introduction

The H_2–NO_2 and H_2–N_2O systems are of interest for a number of reasons. Many of the elementary reactions related to NOx formation/mitigation are key reactions in these simple fuel systems, making them insightful from a fundamental standpoint. From a practical perspective, H_2–NO_2 kinetics are important in rocket-propellant applications [1], while H_2–N_2O kinetics are of interest in safety considerations related to semiconductor manufacturing and nuclear waste management [2].

Emission near 307 nm from excited-state OH (OH^*) corresponding to the $A\ ^2\Sigma^+ \rightarrow X\ ^2\Pi$ transition can serve as a marker of heat release in a variety of fuel/oxidizer systems, and its appearance is often used as an indicator of ignition onset. Furthermore, OH^* emission diagnostics are low-cost and relatively simple to operate. For these reasons, OH^* diagnostics are broadly used across the combustion community and can provide meaningful insights into the kinetics of reacting systems [3].

The H_2–N_2O system has seen a handful of OH^* chemiluminescence studies in shock tubes. Early work involved the low-pressure studies by Soloukhin et al. [4,5] and Hidaka et al. [6]. Soloukhin and Van Tiggelen [4] first proposed the reaction

$$N_2O + H \leftrightarrows N_2 + OH^* \quad (R2)$$

as being responsible for OH^* formation in the H_2–N_2O system. Hidaka et al. then proposed an expression for the rate constant k_2 for R2. The importance of R2 was later corroborated in a number of H_2–N_2O shock-tube studies at higher pressures by Mevel et al. [7–9] and also by Mathieu and Petersen [10]. Mathieu and Petersen used mixtures of NH_3 and O_2 but nonetheless found R2 to be important in predicting the shapes of their OH^* time histories.

While there are studies of H_2–O_2 mixtures sensitized by small amounts of NO_2 (*e.g.*, [11–14]), the present work focuses on H_2 oxidation with NO_2 as the sole oxidizer. In the 1950s, Ashmore and Levitt used a broadband NO_2 absorption diagnostic to study

* Corresponding author.
E-mail address: cmulvihill@tamu.edu (C.R. Mulvihill).

https://doi.org/10.1016/j.combustflame.2019.11.010
0010-2180/

the global ignition behavior of H_2–NO_2 mixtures between 684 and 843 K within a static reactor [15–17]. Concurrently, Rosser and Wise used a similar diagnostic to study H_2–NO_2 oxidation between 600 and 700 K, also within a static reactor [18]. Both Ashmore and Levitt and Rosser and Wise identified important reaction steps in the H_2–NO_2 mechanism, such as $NO_2 + H \leftrightarrows NO + OH$ and $H_2 + OH \leftrightarrows H + H_2O$. Sawyer and Glassman later performed a flow reactor study of H_2–NO_2 oxidation between 850 and 1100 K by measuring temperature profiles using a thermocouple inserted into the flow [19]. More recently, Park et al. studied H_2–NO_2 oxidation between 602 and 954 K in a quartz reactor, measuring NO_2 and NO time histories and ultimately extracting several rate coefficients from their data [20]. Mueller et al. performed a flow reactor study of the H_2–NO_2 reaction by measuring NO, NO_2, and H_2O time histories and provided a single rate coefficient measurement of the reaction $H_2 + NO_2 \leftrightarrows HONO + H$ at 833 K [21].

Several studies of H_2–NO_2 detonation, both experimental and theoretical, have also been performed to investigate the two-step heat release associated with fuel-rich H_2–NO_2 mixtures [22–25]. These detonation studies identified the reaction $NO_2 + H \leftrightarrows NO + OH$ as the primary heat-releasing reaction in both fuel-rich and fuel-lean H_2–NO_2 mixtures. Very recently, Mulvihill et al. utilized H_2O laser absorption to measure H_2O time histories between 917 and 1782 K near 1 atm in dilute H_2–NO_2 mixtures in what seems to be the first shock-tube study of the H_2–NO_2 system [26].

However, there appear to be no studies of OH^* chemiluminescence in the H_2–NO_2 system. Such unique data can further the understanding of H_2–NO_2 kinetics and, as discussed later, can provide insight on chemiluminescent reactions in general. Therefore, the goal of this paper is to provide new OH^* measurements in a shock tube. Presented first are descriptions of the experimental apparatus, with special attention given to H_2–NO_2 mixture preparation. The modeling considerations are then outlined, including new or updated rates for OH^*-quenching reactions. Results for both the H_2–NO_2 and H_2–N_2O mixtures are then presented, followed by a discussion of the new chemiluminescent reaction identified from these data. The proposed OH^* sub-mechanism for the H_2–NO_2 and H_2–N_2O systems is given in tabular form, and comparisons to selected literature data are made.

2. Experiment

2.1. Shock tube

All experiments were performed in a stainless steel shock tube with a driver section of length 3.25 m and inner diameter 7.62 cm with a driven section of length 7.88 m and inner diameter 16.24 cm. Polycarbonate diaphragms of thickness 0.254 mm were burst using He or He/air as the driver gas. The driven section was vacuumed to ultimate pressures of ~10^{-5} Torr prior to each experiment using a turbomolecular pump. Five fast-response, piezoelectric pressure transducers (PCB 113A) were used to track the passage of the incident shock wave and calculate the incident-shock velocity, v_s. The 1-D normal shock wave relations were then used to calculate the temperature (T_5) and pressure (P_5) behind the reflected shock wave using v_s and the measured temperature and pressure of the driven section gas prior to the experiment. Due to uncertainty in v_s, uncertainties in T_5 and P_5 are estimated to be ±0.8% and ±1.0%, respectively. The last PCB transducer (1.6 cm from the endwall) was also used to monitor the sidewall pressure and was shielded using RTV silicone to mitigate heat transfer effects which can alter measured pressure time histories. Time zero was defined by the arrival of the reflected shock wave at the sidewall pressure transducer and was determined with an estimated uncertainty of ±1 μs.

Mixtures were prepared manometrically in a 40-L, stainless steel mixing tank. Partial pressures of constituents were measured using gauges of ranges 0–10 Torr, 0–1000 Torr, or 0–13,000 Torr. Prior to mixture preparation, the mixing tank was vacuumed to ultimate pressures of ~10^{-6} Torr using the turbomolecular pump. After mixture preparation, mixtures were allowed to mix for at least 60 min prior to experiments. Gases were supplied by Praxair with the following purity levels: 99.999% for Ar, 99.999% for H_2, 99.5% for N_2O, and 99.5% for NO_2. The NO_2 was supplied as a mixture of 1.03% NO_2 in balance Ar; this NO_2–Ar mixture was used to prepare all mixtures containing NO_2. The composition of the H_2–NO_2 mixture was 0.222% H_2/0.392% NO_2/99.386% Ar ($\varphi = 0.28$), while the composition of the H_2–N_2O mixture was 0.333% H_2/0.666% N_2O/99.001% Ar ($\varphi = 0.50$).

2.2. LED-based NO_2 diagnostic

In a recent study by the authors [26], it was observed that H_2–NO_2 mixtures were found to contain less NO_2 than expected according to partial pressure calculations. It was originally suspected this lower-than-expected NO_2 concentration was due to NO_2 dimerization to N_2O_4 (i.e., $2NO_2 \rightleftarrows N_2O_4$). Regardless of the mechanism causing the lower NO_2 concentration, the authors chose for the present study to simply measure the amount of NO_2 in the final mixture directly. To assess the mixture concentrations, Mulvihill et al. [26] employed two methods of determining the NO_2 concentration: an inference method using a laser absorption diagnostic for H_2O and a direct measurement method using an LED-based diagnostic for NO_2. The LED diagnostic was described briefly by Mulvihill et al. and is described in more detail below. The two diagnostics demonstrated excellent agreement in terms of the NO_2 mole fraction in the mixtures. Note that the H_2O diagnostic also served to validate the accurate H_2 content of the H_2–NO_2 mixtures used by Mulvihill et al., one of which was nearly identical to the H_2–NO_2 mixture used herein.

A blue LED was supplied by a benchtop power supply at 3.5 V and ~70 mA. LED light traversed an 11.74-cm aluminum absorption cell with sapphire windows and terminated on a silicon photodetector (Newport 2032) operated with a gain of 2×10^6 V/A; the slight detector voltage offset was subtracted from the measured intensity to obtain the true intensity. A series of collimating lenses was employed, and an aperture eliminated stray light. A bandpass filter with center wavelength $\lambda_c = 459$ nm and full-width at half-maximum FWHM = 5 nm was also placed in the beam path. The spectral density of the filtered LED light was measured with a spectrometer (Ocean Optics HR2000+) as shown in Fig. 1. The spectrometer was calibrated using a Hg/Ar pen lamp (Oriel 6035).

N_2O_4 presents a negligible level of absorption near 460 nm, making this LED ideal for NO_2 measurements that are free from N_2O_4 interference (Fig. 1). Although the absorption coefficients (k_ν) in Fig. 1 were not obtained using Ar as the bath gas, prior work [29] has demonstrated that k_ν for NO_2 in this region is insensitive to pressure in the range of interest (0 to ~250 Torr), suggesting that the identity of the collisional partner has a negligible effect on k_ν. The product of the NO_2 spectrum and the LED spectrum (normalized to an area of 1) was integrated to obtain an effective k_ν of 10.59 cm^{-1} atm^{-1}.

To validate k_ν, a calibration mixture of 1.03% NO_2/Ar was utilized. This mixture was prepared by Praxair using the gravimetric method, which is insensitive to N_2O_4 dimerization. The absorbance A was measured by recording the light intensity on the photodetector with (I_t) and without (I_0) varying pressures of mixture in the absorption cell using the Beer-Lambert law $A = -\ln(I_t/I_0)$. A is defined as $A = k_\nu P X_{abs} L$, where P is the pressure, X_{abs} is the mole fraction of the absorbing species, and L is the path length. The val-

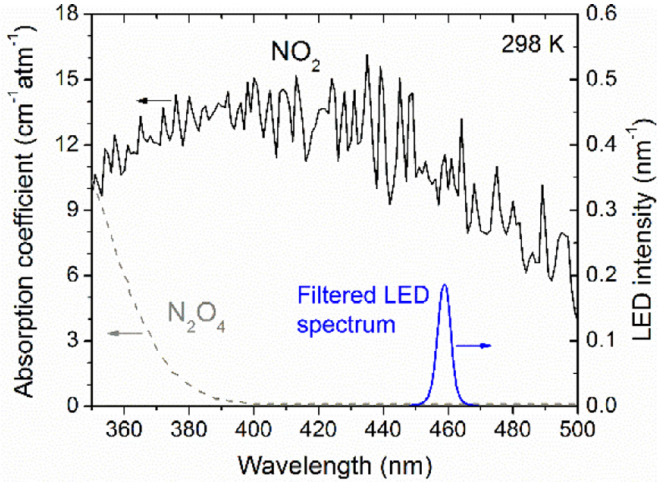

Fig. 1. Literature values of room-temperature absorption coefficients of NO_2 [27] and N_2O_4 [28]. The measured spectrum of the filtered LED (normalized to an area of 1) is also shown.

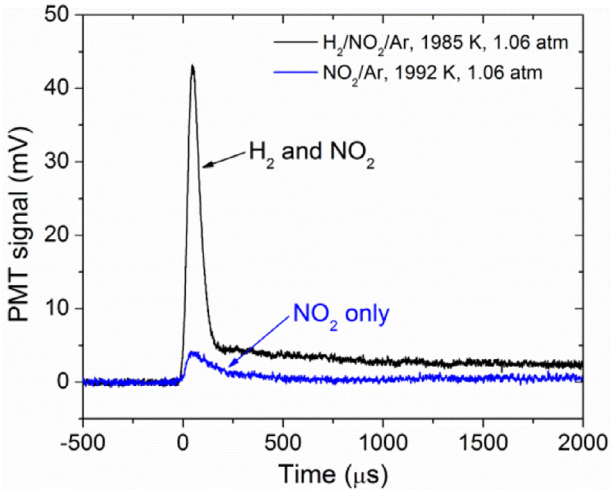

Fig. 3. Comparison of raw PMT signals with (0.222% H_2/0.392% NO_2/Ar) and without (0.392% NO_2/Ar) H_2 in the mixture. Identical optical configurations were used for both experiments (bandpass filter: λ_c = 300 nm, FWHM = 40 nm).

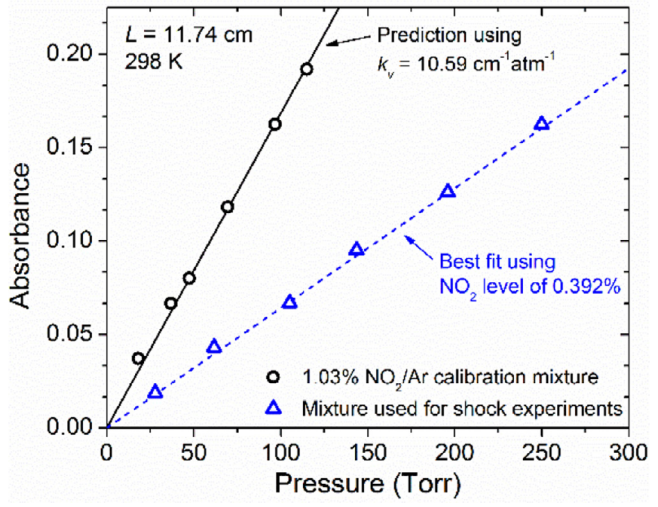

Fig. 2. Room-temperature absorbance of NO_2-containing mixtures using the LED diagnostic. Symbols: measured values, solid line: prediction using k_v = 10.59 $cm^{-1}atm^{-1}$ and X_{abs} = 1.03%, dashed line: best fit to measured data obtained using k_v = 10.59 cm^{-1} atm^{-1} and X_{abs} = 0.392%. Uncertainty bars (±2%, assuming ±1 mV uncertainty in I_t and I_0) are smaller than symbols.

ues of A measured in the calibration mixture and the prediction of A using X_{abs} = 1.03% and k_v = 10.59 cm^{-1} atm^{-1} typically agreed within 1% (Fig. 2), validating the calculated k_v. Another calibration with a known mixture of 1.02% NO_2/Ar further confirmed the calculated k_v.

Figure 2 also shows the measured absorbance data for the mixture used during shock-tube experiments as well as the best fit to these data, which was obtained using X_{abs} = 0.392% and k_v = 10.59 cm^{-1} atm^{-1}. The value of 0.392% was therefore used as the NO_2 mole fraction for the H_2/NO_2/Ar mixture, with a conservatively estimated uncertainty of ±4%. The expected NO_2 concentration in this mixture, based on partial pressure calculations, was 0.444%. The final mixture composition was 0.222% H_2/0.392% NO_2/Ar. As mentioned earlier, the NO_2 and H_2 compositions in H_2/NO_2/Ar mixtures were confirmed by the authors in a separate work via direct measurements using the NO_2 diagnostic and via indirect measurements using an H_2O laser absorption diagnostic. The two diagnostics demonstrated excellent agreement regarding the NO_2 content in the mixtures; see Mulvihill et al. [26] for more details.

Even at 250 Torr, room-temperature chemical equilibrium calculations indicate that the mole fraction of N_2O_4 is only 2.2% that of NO_2, which is well within the ±4% uncertainty. This minimal influence of dimerization on the measurements in Fig. 2 decreases with pressure: the calculated amount of N_2O_4 drops to 0.9% of the NO_2 mole fraction at 100 Torr. Therefore, NO_2 dimerization had a minimal impact on the NO_2 measurements in the absorption cell.

2.3. OH* diagnostic

Light emission from the shock tube exited a sapphire window port located 1.6 cm from the endwall (in the same plane as the sidewall pressure transducer). After passing through a 2.0-mm slit (1.5 mm for the H_2–N_2O experiments due to higher signal levels), the light was focused via a mirror (f = 25 cm) and lens (f = 10 cm) onto a photomultiplier tube (PMT) (Hamamatsu 1P21). The PMT was supplied by a power supply at voltages between 500 and 830 V; care was taken to keep the output of the PMT below the linearity limit associated with the selected power supply voltage. The PMT was fitted with a bandpass filter: λ_c = 300 nm, FWHM = 40 nm for the H_2–NO_2 experiments due to low emission levels and λ_c = 307 nm, FWHM = 10 nm for the H_2–N_2O experiments. Data obtained at lower temperatures were digitally filtered during post-processing to remove electrical noise due to low signal levels.

2.4. NO_2 interference

Although previous works on high-temperature NO_2 emission suggest that NO_2 emission declines rapidly below 330–390 nm [30,31], several checks were performed to characterize such emission. Figure 3 shows the raw PMT voltage obtained by shock-heating the H_2/NO_2/Ar mixture used herein. A mixture with no H_2 was then shock-heated to similar conditions using the same optical setup. A small amount of NO_2 interference was observed at this wavelength; the NO_2 emission in Fig. 3 is ~9% of the OH* signal. A similar pair of experiments were performed at ~2050 K, and the NO_2 emission at this higher temperature was ~14% of the OH* signal, suggesting that the NO_2 interference increased with temperature. Since the conditions of Fig. 3 were at the high-temperature end of this study, the upper limit on NO_2 interference in the measured OH* profiles was conservatively 10%, although it was likely

Table 1
The OH* sub-mechanism used in the present study. Reaction rates given in the form $k = AT^n \exp(-E_a/RT)$. Units are cal, mol, cm^3, and s.

No.	Reaction	A	n	E_a	Reference
1	NO_2+H ⇆ NO+OH*	7.00×10^{13}	0	55,000	This study
2	N_2O + H ⇆ N_2 + OH*	1.60×10^{14}	0	50,300	[6]
3	O + H (+M) ⇆ OH* (+M)	1.50×10^{13}	0	5975	[34]
4	H + OH* ⇆ H + OH	1.31×10^{13}	0.5	−167	[35]
5	H_2 + OH* ⇆ H_2 + OH	2.95×10^{12}	0.5	−445	[35]
6	H_2O + OH* ⇆ H_2O + OH	5.93×10^{12}	0.5	−862	[35]
7	N_2 + OH* ⇆ N_2 + OH	1.08×10^{11}	0.5	−1240	[35]
8	OH + OH* ⇆ OH + OH	6.01×10^{12}	0.5	−763	[35]
9	O_2 + OH* ⇆ O_2 + OH	2.10×10^{12}	0.5	−483	[35]
10	Ar + OH* ⇆ Ar + OH	1.30×10^{10}	0.5	−199	This study
11	NH_3 + OH* ⇆ NH_3 + OH	9.00×10^{12}	0.5	−596	This study
12	N_2O + OH* ⇆ N_2O + OH	6.00×10^{12}	0.5	−556	This study
13	NO + OH* ⇆ NO + OH	6.00×10^{12}	0.5	−397	This study
14	NO_2 + OH* ⇆ NO_2 + OH	6.00×10^{12}	0.5	−556	This study[a]
15	OH* → OH	1.45×10^{6}	0	0	[36]

[a] Assumed to be the same as for N_2O.

much less than this at lower temperatures. The NO_2 emission was not thermal, as confirmed by an emission check at 335 nm that revealed no emission; see Fig. S10 of the Supplementary Material (SM). It is worth noting the H_2–NO_2 and NO_2 systems possess different O-atom time histories (according to numerical predictions), so the comparison of the two systems may not be valid. However, the comparison shown in Fig. 3 seemed to be the best option available to the authors.

As another check for NO_2 interference, a comparison between two bandpass filters (λ_c = 307 nm, FWHM = 10 nm and λ_c = 300 nm, FWHM = 40 nm) was performed; see Fig. S11 of the SM. The shapes of the two normalized OH* profiles were very similar, and the small differences observed were likely due to slight differences in T_5 and P_5. The similar time histories demonstrated that the NO_2 interefence did not significantly alter the shapes of the measured emission profiles and also justified the use of the filter with FWHM = 40 nm.

3. Modeling

Modeling was performed using the Closed Homogenous Batch Reactor within the CHEMKIN software suite. The constant-internal energy, constant-volume assumption was utilized, which produces identical results to the constant-enthalpy, constant-pressure assumption for the dilute mixtures used herein. The recent modeling work of Zhang et al. [32] was chosen as the base NOx mechanism, with the minor modifications proposed by Mulvihill et al. [2,33]. The OH* sub-mechanism included by Zhang et al. was replaced with that of the current study, which is given in Table 1. Kinetic data on OH* includes three types of reactions that are discussed below: OH*-forming (i.e., chemiluminescent) reactions, OH*-quenching reactions, and radiative decay. These three classes of reactions can also be generalized to other chemiluminescent species (e.g., CH*).

3.1. OH*-forming reactions ($A + B \leftrightarrows C + OH^*$)

Reactions that result in the formation of OH may possess an analogous OH*-forming (i.e., chemiluminescent) reaction. The chemiluminescent reactions considered in the present study were

$$NO_2 + H \leftrightarrows NO + OH^* \quad (R1)$$

$$N_2O + H \leftrightarrows N_2 + OH^* \quad (R2)$$

$$O + H\ (+M) \leftrightarrows OH^*\ (+M). \quad (R3)$$

The rates for R2 and R3 were taken from Hidaka et al. [6] and Kathrotia et al. [34], respectively, while R1 is proposed in this study for the first time.

3.2. OH*-quenching reactions ($OH^* + A \leftrightarrows OH + A$)

OH* can return to the $X\,^2\Pi$ ground state via collisional quenching by other molecules. Many data exist on OH* quenching by various molecules, and the review by Tamura et al. [35] provides fits to such data. In the present work, quenching rates for H, H_2, H_2O, N_2, OH, and O_2 were taken directly from Tamura et al.

Ar is often used as a bath gas in shock-tube experiments, but an expression for OH* quenching by Ar was not given by Tamura et al. [35]. In the present study, an expression was fit to the available quenching data for Ar that accounts for both the high- and low-temperature literature data for quenching by Ar (Fig. 4(a)). Additionally, due to the present interest in modeling H_2–NO_2 and H_2–N_2O chemistry, reactions for OH* quenching by NO, NH_3, and N_2O were fitted to literature data (Fig. 4(b)–(d)). No data on OH* quenching by NO_2 could be found, so the OH* quenching for NO_2 was assumed to be equal to that for N_2O. The rates for all quenching reactions in Table 1 follow similar trends (n = 0.5, E_a < 0) based upon the harpooned collisional complex model of Paul [37].

In their Table 2, Kathrotia et al. [34] erroneously transcribed the pre-exponential factor of k_4 (H quenching) from Tamura et al. [35] (although Fig. 1(a) of Kathrotia et al. correctly plots k_4). However, calculations at the conditions of the absolute OH* calibration used by Kathrotia et al. (3000 K, 2 atm, 1% H_2/1% O_2/Ar) using their H_2–O_2 mechanism showed only a 1.8% change in the OH* level when using the correct versus incorrect value of k_4. Consequently, even if Kathrotia et al. did use the incorrect value of k_4, it would have had a negligible effect on their OH* calibration, and so the conclusions of Kathrotia et al. seem reliable. The correct k_4 parameters from Tamura et al. [35] are given in Table 1.

3.3. Radiative decay ($OH^* \rightarrow OH$)

OH* can also return to the $X\,^2\Pi$ ground state via spontaneous emission. The observed OH* emission is due to this process. The radiative lifetime of OH* was taken from Dimpfl and Kinsey [36].

4. Results

4.1. H_2–NO_2 experiments

Figure 5 shows several normalized OH* profiles from the H_2–NO_2 mixture. The dashed lines indicate predictions of the

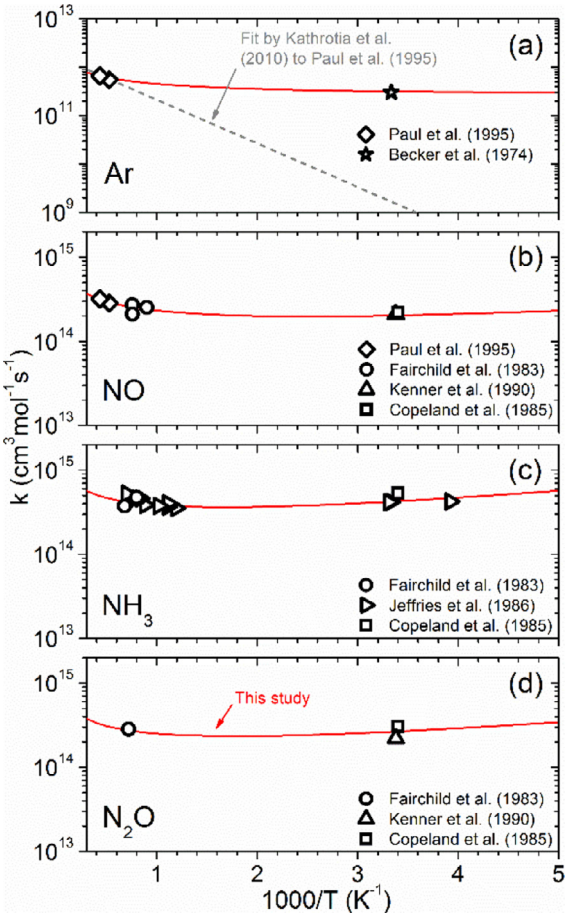

Fig. 4. Rate coefficients of quenching of the OH $A\ ^2\Sigma^+$ state by (a) Ar, (b) NO, (c) NH_3, and (d) N_2O. Symbols: experimental data, solid lines: fits used in this study, dashed line: fit used by Kathrotia et al. [34]. Data are from Paul et al. [38], Becker et al. [39], Fairchild et al. [40], Kenner et al. [41], Copeland et al. [42] (rotational quantum number $N = 0$), and Jeffries et al. [43].

Zhang et al. mechanism [32] supplemented with the current OH* sub-mechanism but without R1 included. These predictions exhibit large deficiencies, particularly at higher temperatures. However, when the best-fit R1 is included in the model, the predictions are strikingly improved. The presence/absence of R2 in the mechanism had no effect on these predictions since there is a negligible amount of N_2O produced in this mixture. Additional experimental data are provided in the SM, and the considerations used in the fitting of k_1 are described in Section 5.1.

Figure 6(a) shows the peak OH* values from the H_2–NO_2 tests. Since an absolute OH* calibration was not performed in this study, the peak OH* values were normalized to the hottest run (2003 K). To ensure accurate relative OH* values, differences in PMT amplification were accounted for, and care was taken to ensure that the optical setup remained undisturbed during these tests. Figure 6(b) shows the time required for the OH* to decrease to 50% of the peak value. Also shown in Fig. 6 are the same model predictions as in Fig. 5. With the addition of R1, the peak OH* values are moderately improved while the time to 50% reductions are significantly improved, particularly at higher temperatures. Since quantitative observations are masked by normalization in Fig. 6(a), it is worth noting that the predicted absolute peak OH* values of the solid line are ~10 times higher than those of the dashed line at the high-temperature extreme.

For the H_2–NO_2 experiments, a slight amount of OH* emission was observed prior to the arrival of the reflected shock wave, particularly for the hotter experiments (almost no such effects were observed for the H_2–N_2O experiments due to both the lower shock-wave velocity and the smaller slit width). A sample case of this premature emission is illustrated in Fig. 7. Considerations of the PMT supply voltages and the calculated post-incident-shock conditions (T_2 and P_2) revealed that the premature emission was not due to OH* formation at T_2 and P_2 but was rather due to convolution of the OH* emission with the relatively wide slit (i.e., due to OH* emission from the region upstream of the window port). To consider the effect of this convolution, model predictions were convolved with a Gaussian profile to represent the temporal slit function created by the reflected shock wave relative to the stationary PMT optics, as shown in Fig. 7. The convolved model in Fig. 7 generally resembles the experimentally observed premature emission. Furthermore, the convolution brings the model into slightly better agreement with the data by shifting the timing of the peak OH* closer to the data and also slightly smoothing out the dip in OH* that is not observed in the data.

It may be possible to deconvolve the experimental data to obtain OH* profiles that are unaffected by slit effects. However, such deconvolution was not pursued for two reasons. First, the unavoidable noise fluctuations in the experimental OH* profiles are greatly magnified upon deconvolution. While a Wiener filter [44] can be used to overcome some of these noise magnifications, initial attempts with a Wiener filter produced unsatisfactorily noisy deconvolved profiles. Second, the case shown in Fig. 7 is the highest-temperature experiment for which the reflected shock speed is a maximum and, therefore, the convolution effects are a maximum. However, even in this worst-case scenario, the convolution effects are quite minor. Ultimately, slit convolution effects had no impact on the best-fit k_1 from the present study.

4.2. H_2–N_2O experiments

Figure 8 shows several normalized OH* profiles from the H_2–N_2O mixture. The dashed lines indicate predictions of the Zhang et al. mechanism [32] supplemented with the current OH* sub-mechanism, but with R1 excluded. When the best-fit R1 is included (solid lines), the predictions are completely unchanged so that the two mechanism predictions are indistinguishable. Figure 9(a) shows the peak OH* values that have been normalized to the hottest run (1776 K), while Fig. 9(b) shows the time required to reach the peak OH*. As in Fig. 8, the two mechanism predictions in Fig. 9 are indistinguishable, demonstrating that the addition of the best-fit R1 to the mechanism has no effect on OH* kinetics in the H_2–N_2O system at these conditions.

5. Discussion

5.1. Fitting of $NO_2 + H \leftrightarrows NO + OH^*$ (R1)

Chemiluminescence is strongly associated with heat release [3], and, in some cases, may be produced by a reaction with a ground-state analog that is a primary heat-releasing reaction. For example, the ground-state reaction $N_2O + H \leftrightarrows N_2 + OH$ is known to be the primary source of heat release during the oxidation of H_2–N_2O mixtures [8,25,45], and the chemiluminescent form of this reaction, R2, has been identified as the primary source of OH* in H_2–N_2O mixtures [5,6,8]. By analogy to R2, the new chemiluminescent reaction R1 was postulated based on the known importance of its ground-state analog, $NO_2 + H \leftrightarrows NO + OH$, to heat release in H_2–NO_2 mixtures [22,24,25]. It should be noted that the association with heat release is not the case for every chemiluminescent reaction. For example, the reactions $CH + O_2 \rightleftarrows OH + CO$, $C_2 + OH \rightleftarrows CH + CO$, and $C_2H + O \rightleftarrows CH + CO$ are unimportant for heat release yet they possess chemiluminescent analogs.

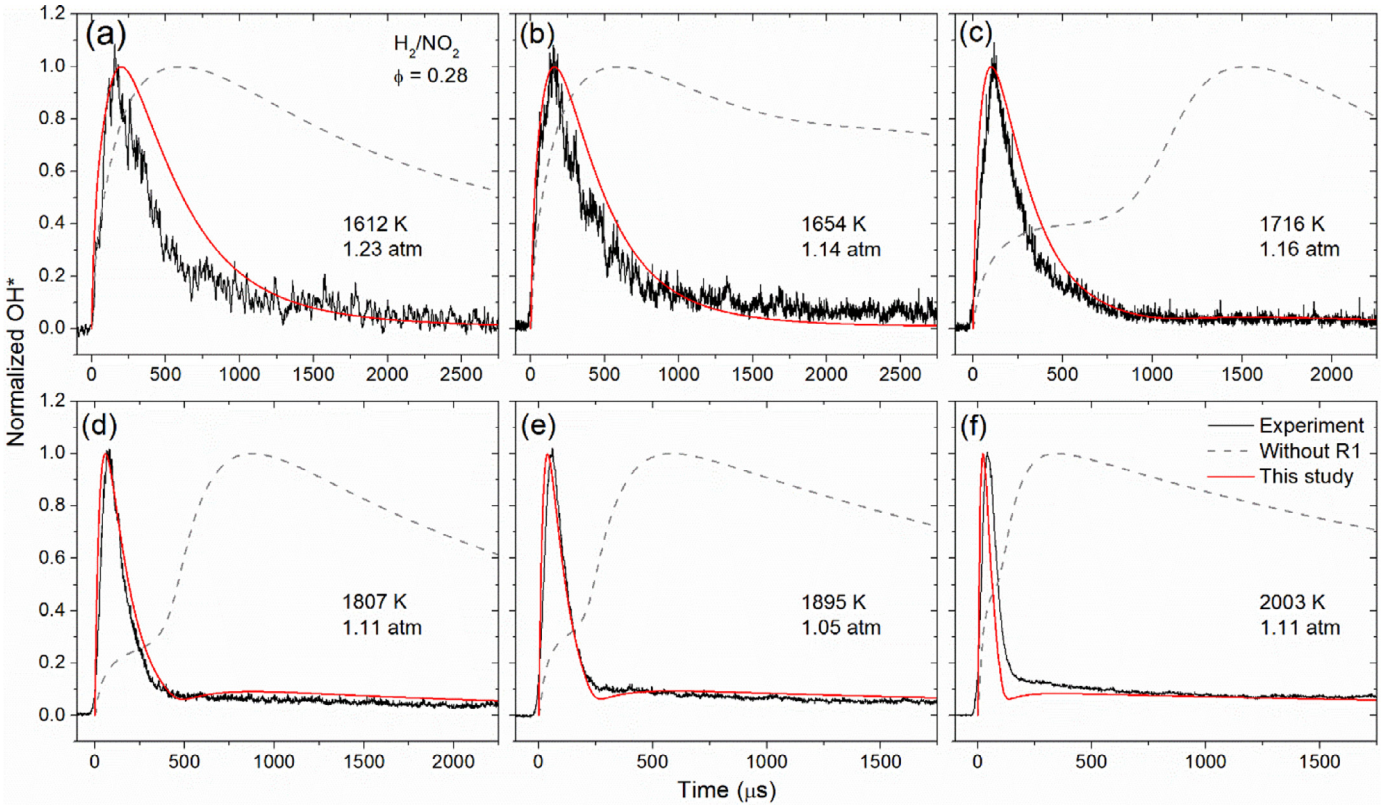

Fig. 5. Normalized OH* profiles in a mixture of 0.222% H_2/0.392% NO_2/Ar. Thick solid lines: mechanism of [32] plus the OH* sub-mechanism of this study, dashed lines: [32] plus the OH* sub-mechanism of this study with R1 removed.

Using the Zhang et al. [32] mechanism as the base NOx mechanism, the pre-exponential factor A for k_1 was determined by matching the model predictions to the shapes of the experimental OH* time histories (Fig. 5), while the best-fit activation energy E_a was determined by matching the model predictions to the slope of the normalized peak OH* data (Fig. 6(a)). The sensitivity of the OH* predictions to the value of k_1 is demonstrated in Fig. 10. The value of k_1 affects the amount of peak OH* produced, which indirectly affects the shape of the profile in the tail region due to normalization of the OH* profile.

The collision limits for the forward and backward rate coefficients of R1 were calculated using the hard-sphere data from Svehla [46] and are compared to the best-fit forward and backward rate coefficients of R1, k_{1f} and k_{1b}, in Fig. 11. k_{1b} is faster than k_{1f} across the temperature range of the present study since R1 is highly endothermic ($\Delta H_R^0 = 64.4$ kcal/mol), making violation of the collision limit of concern for k_{1b}. However, Fig. 11 shows that in the temperature range of the present study, k_{1b} remains a factor of 20 below the backward collision limit. The negative activation energy of k_{1b} in Fig. 11 is characteristic of reactions for which ΔH_R^0 exceeds E_a. Additionally, k_{1f} (i.e., k_1) is ~7 orders of magnitude slower than its ground-state counterpart ($NO_2 + H \leftrightarrows NO + OH$); this is in general accord with R2 and R3, whose rate constants are respectively ~4 and ~3 orders of magnitude slower than their ground-state counterparts in the temperature range of the present study.

The evolution of the OH* profiles in the present H_2–NO_2 experiments can be explained by investigating the predicted time histories of H, O, and NO_2, which are shown in Fig. 12(a) for a sample case. A rate-of-production analysis using the Zhang et al. [32] mechanism revealed H is formed initially by $H_2 + O \leftrightarrows H + OH$ and then later by $H_2 + OH \leftrightarrows H + H_2O$, and is consumed almost exclusively by $NO_2 + H \leftrightarrows NO + OH$. Oxygen atoms are formed immediately by NO_2 (+M) $\leftrightarrows$ NO + O (+M) and, to a much lesser extent, by NO_3 (+M) $\leftrightarrows$ NO_2 + O (+M). O-atom consumption arises primarily from the reactions $NO_2 + O \leftrightarrows NO + O_2$ and $H_2 + O \leftrightarrows H + OH$. At later times (~600 μs for the case in Fig. 12(a)), a slight increase in O-atom production arises from the reaction $O + H_2O \leftrightarrows OH + OH$ in reverse. NO_2 consumption begins immediately due to NO_2 (+M) $\leftrightarrows$ NO + O (+M), but the reaction $NO_2 + H \leftrightarrows NO + OH$ quickly becomes the dominant pathway for NO_2 destruction. The reaction $NO_2 + O \leftrightarrows NO + O_2$ also plays a small role in NO_2 consumption.

As highlighted in Fig. 12(b), the OH* production at early times originates from R1. As the NO_2 concentration decreases rapidly, OH* production by R1 concomitantly decreases. The increases in O and H concentrations at later times cause a slight rise in OH* concentration due to OH* production by R3.

5.2. Effect of R1 on the modeling of the H_2–N_2O system

A matter of potential concern was that the modeling of data in the H_2–N_2O system would be degraded upon the introduction of R1 to the kinetic mechanism. However, this concern for diminished performance with N_2O as the oxidizer was found to be unwarranted. Figures 8 and 9 demonstrate the lack of effect of R1 on modeling of the H_2–N_2O data from the present study: the mechanism predictions with and without R1 are identical. Further evidence of the lack of effect of R1 on modeling H_2-N_2O kinetics was found by utilizing the absolute peak OH* data of Hidaka et al. [6]. Hidaka et al. acquired quantitative peak OH* data in three H_2–N_2O mixtures, which are shown in Fig. 13. Also shown in Fig. 13 are the model predictions of the current study both with and without R1 included in the mechanism. In an identical fashion to

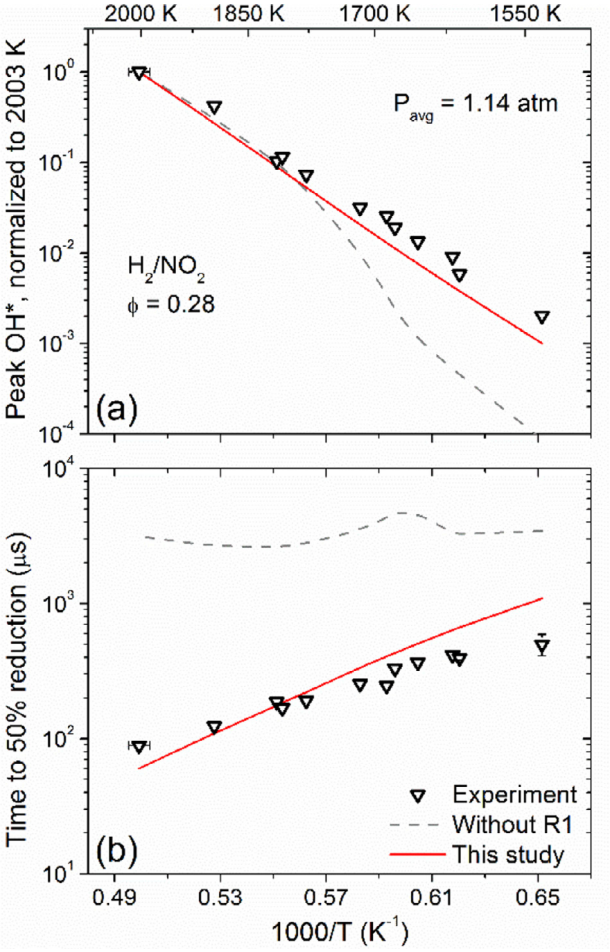

Fig. 6. (a) Normalized peak OH* values and (b) time to 50% reduction values in a mixture of 0.222% H_2/0.392% NO_2/Ar. Solid lines: mechanism of [32] plus the OH* sub-mechanism of this study, dashed lines: [32] plus the OH* sub-mechanism of this study with R1 removed. *Y*-axis uncertainty bars are (a) ±15% and (b) experiment-specific and are smaller than the symbols if not visible.

Figs. 8 and 9, the two model predictions in Fig. 13 are identical, further demonstrating the introduction of R1 into the mechanism has no effect on the modeling of these H_2–N_2O data. The inclusion of R1 was also found to have no effect on modeling of OH* data in the NH_3–O_2 system; see the SM for details.

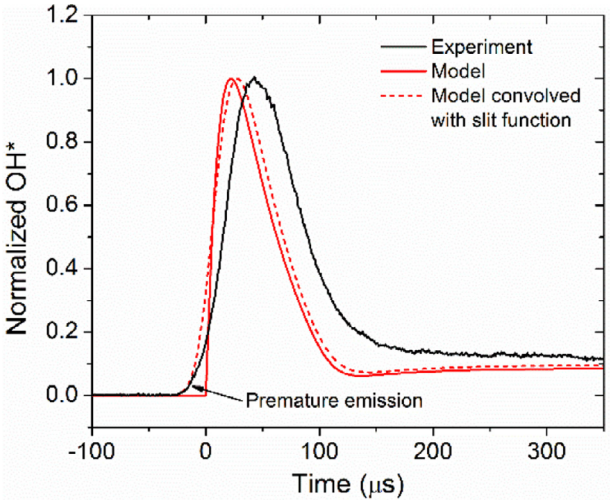

Fig. 7. Effect of convolving the model predictions with a slit function. Thick solid line: mechanism of [32] plus the OH* sub-mechanism of this study, short dashed line: [32] plus the OH* sub-mechanism of this study convolved with a Gaussian slit function with FWHM = 26 μs. Conditions and experimental data are those of Fig. 5(f) (2003 K, 1.11 atm).

5.3. Mechanism-dependent nature of fitting k_1

An unavoidable aspect of the k_1 fitting is its mechanism-dependent nature; similar dependences have been discussed, for example, by Kathrotia et al. [34]. To demonstrate this mechanism dependence, a repeat fitting of k_1 was performed using Glarborg et al. [47] as the base mechanism. The best-fit k_1 using the Glarborg et al. mechanism was 5 times lower than the best-fit k_1 obtained with the Zhang et al. [32] mechanism. This difference in the best-fit k_1 resulted primarily from differences in predictions of H-atom concentrations and also O-atom concentrations due to different rate coefficients employed by Zhang et al. and Glarborg et al. Sensitivity analyses at the conditions of Fig. 10 using both mechanisms revealed that predictions of H, O, and NO_2 are all chiefly sensitive to the reaction NO_2 (+M) ⇆ NO + O (+M) in the first ~500 μs. Zhang et al. utilized the rate constant from Tsang and Herron [1], while Glarborg et al. recommend the expression from Yarwood et al. [48] for M = Ar. The two expressions are identical to within 1% at the low-temperature end of the present study but the Yarwood et al. expression is 30% larger at the high-temperature end of the present study. Further details on the differences between Zhang et al. and Glarborg are provided in the SM. The Zhang

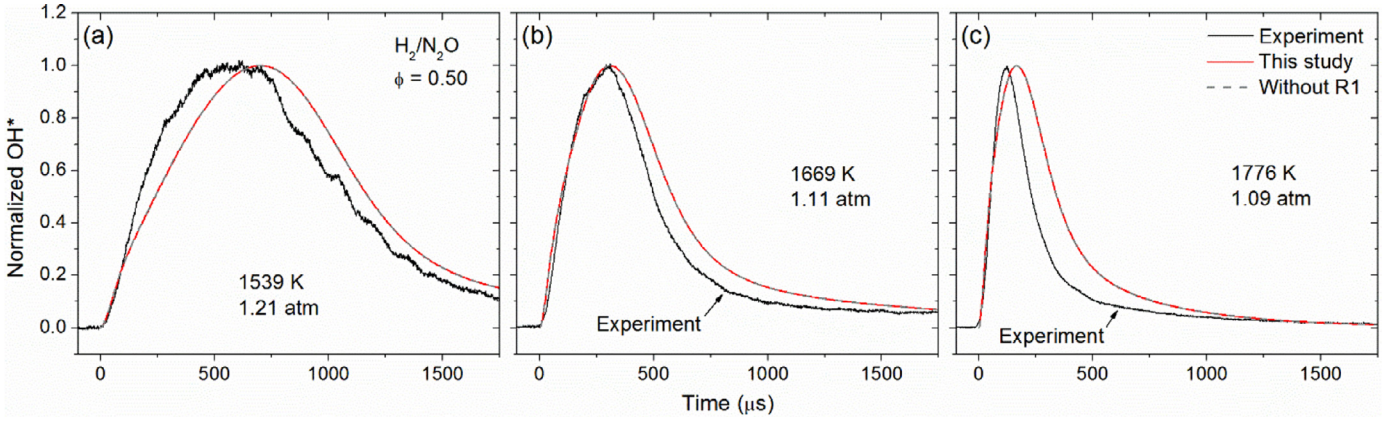

Fig. 8. Normalized OH* profiles in a mixture of 0.333% H_2/0.666% N_2O/Ar. Thick solid lines: mechanism of [32] plus the OH* sub-mechanism of this study, dashed lines: [32] plus the OH* sub-mechanism of this study with R1 removed. The two mechanism predictions are indistinguishable.

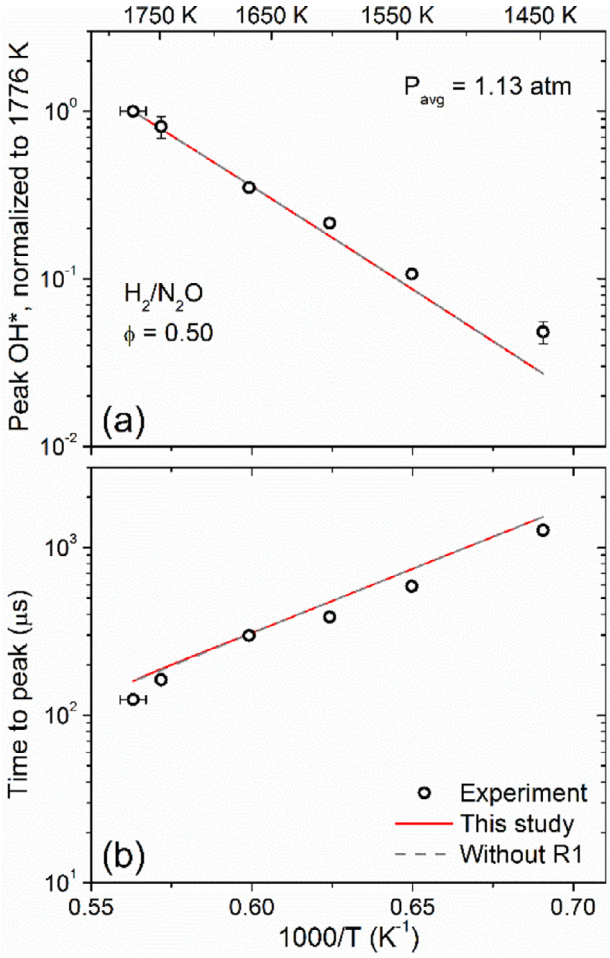

Fig. 9. (a) Normalized peak OH* values and (b) time-to-peak values in a mixture of 0.333% H_2/0.666% N_2O/Ar. Solid lines: mechanism of [32] plus the OH* sub-mechanism of this study, dashed lines: [32] plus the OH* sub-mechanism of this study with R1 removed. *Y*-axis uncertainty bars are (a) ±15% (two representative values shown) and (b) experiment-specific (smaller than the symbols). The two mechanism predictions are indistinguishable.

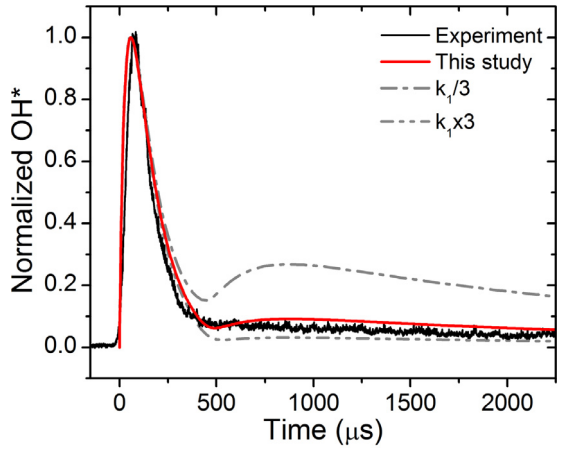

Fig. 10. Effects of varying k_1. Conditions are 1807 K, 1.11 atm in a mixture of 0.222% H_2/0.392% NO_2/Ar. Thick solid, dash–dot, and dash–dot–dot lines: mechanism of [32] plus the OH* sub-mechanism of this study, with the changes to k_1 as indicated.

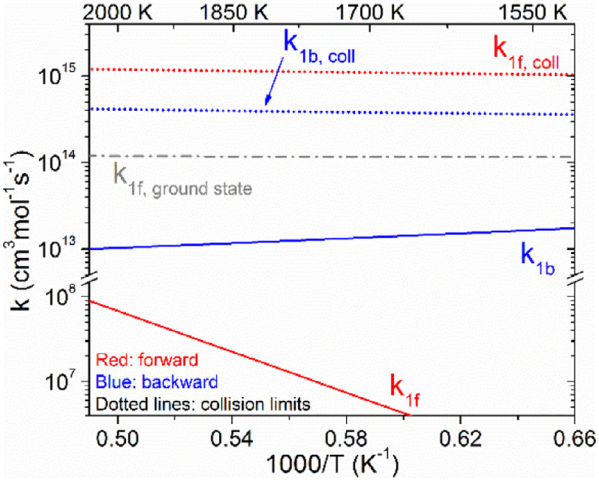

Fig. 11. The best-fit forward and backward rate constants (solid lines) and the calculated forward and backward collisional limits (dotted lines) for R1. The dash–dot line shows the forward rate constant for the ground-state reaction NO_2+H ⇆ NO+OH using the expression employed by Zhang et al. [32]. The hard-sphere diameter for NO_2 was not given by Svehla [46] but was conservatively estimated to be the same as for NO.

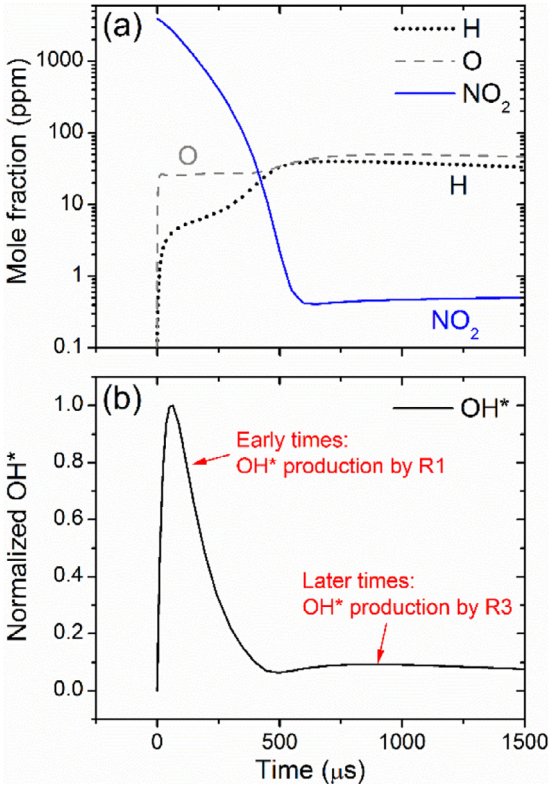

Fig. 12. Numerical predictions of (a) H, O, and NO_2 and (b) OH* concentrations during H_2-NO_2 oxidation. Calculated using the mechanism of Zhang et al. [32] plus the OH* sub-mechanism of this study. Conditions are 1807 K, 1.11 atm in a mixture of 0.222% H_2/0.392% NO_2/Ar.

et al. mechanism was ultimately chosen as the base mechanism in the present study since the agreement with the experimental data was improved over that of the Glarborg et al. mechanism; see the SM for a demonstration of the best fit obtained with Glarborg et al.

An additional source of mechanism dependence is the rate constant for the chemiluminescent reaction R3. The value of k_3 proposed by Hall and Petersen [49] was tested during the fitting of k_1. This rate is 5.4 and 7.5 times greater than the Kathrotia et al.

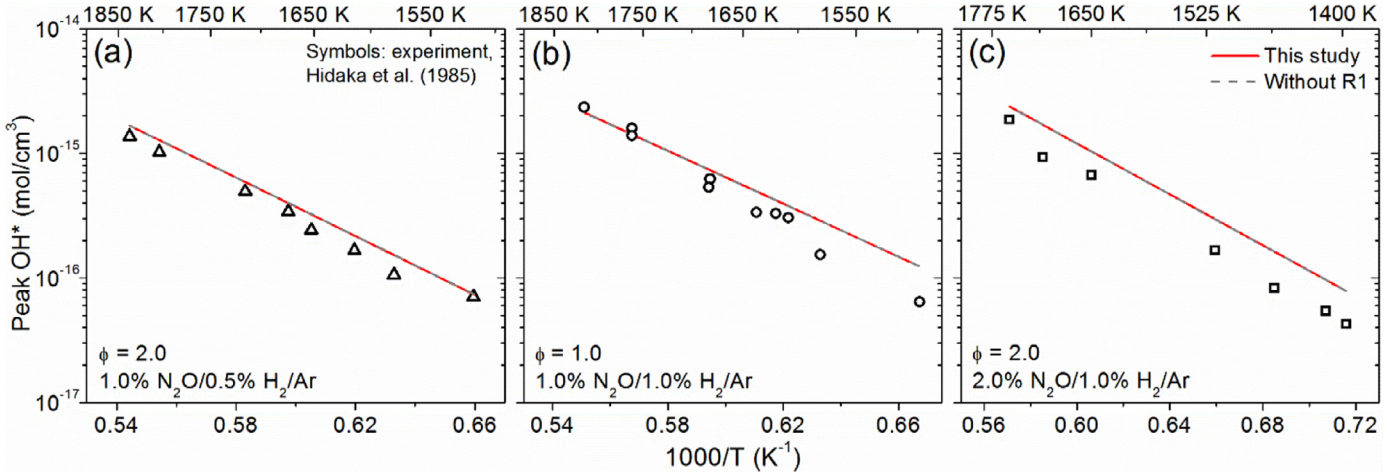

Fig. 13. Quantitative peak OH* levels in three H_2-N_2O mixtures. Symbols: experiments from Hidaka et al. [6], solid lines: mechanism of [32] plus the OH* sub-mechanism of this study, dashed lines: [32] plus the OH* sub-mechanism of this study with R1 removed. The two mechanism predictions are indistinguishable. The average pressure was not explicitly given by Hidaka et al. but was assumed to be 2 atm.

[34] rate at the low- and high-temperature ends of this study, respectively. Employing the Hall and Petersen value for k_3 would produce a best-fit k_1 nearly an order of magnitude higher than was obtained using the Kathrotia et al. value for k_3 due to higher OH* production in the tails of the profiles. This larger best-fit k_1 would bring the backward rate constant of k_1 much closer to the backward collision limit (Fig. 11). To keep the backward rate constant well below its collision limit in the temperature range of the present study, the authors chose to use the Kathrotia et al. value of k_3.

5.4. Energetic considerations for chemiluminescent reactions

Since at least 1951 [50], a common practice in searching for possible chemiluminescent reactions has been to only consider reactions for which the standard-state heat of reaction (ΔH_R^0) of the ground-state form of the reaction exceeds the ΔE associated with the wavelength of the chemiluminescence. For emission at wavelength λ, the associated ΔE is given by $\Delta E = -N_A hc/\lambda$, where N_A is Avogadro's number, h is Planck's constant, and c is the speed of light. Assuming $\lambda = 305 \pm 7$ nm for the OH $A \rightarrow X$ band, ΔE is -93.9 ± 2.1 kcal/mol. ΔH_R^0 for the ground-state forms of both R1 (-29.5 kcal/mol) and R2 (-62.9 kcal/mol) are well below this limit, as illustrated in Fig. 14. The presence of R2 has been repeatedly confirmed by previous studies (Section 1), while R1 is being proposed herein for the first time. The original paper of Soloukhin [4] suggested R2 but did not comment on its endothermicity, while Hidaka et al. [6] briefly mentioned the endothermicity of R2. The present results support the endothermicity of R2.

In light of the large exothermicity of the other well-known chemiluminescent reactions, a search of the exothermic, OH-producing reactions in the NOx kinetic system was conducted. However, even considering reactions with $\Delta H_R^0 \geq -50$ kcal/mol, none of the proposed chemiluminescent reactions other than R1 were able to suitably model the experimental while also remaining below the forward and backward collision limits (see the SM for more details on exothermic, OH-producing reactions and the attempted fitting with such reactions). Furthermore, out of the exothermic, OH-producing reactions in the NOx system, only $NO_2 + H \rightleftarrows NO + OH$ is known to be strongly correlated with heat release. Therefore, R1 seems to be the strongest candidate for the OH* formation observed in the H_2–NO_2 experiments.

The notion that ΔH_R^0 should exceed ΔE follows from simple intuition. However, such a stipulation does not account for the existence of energetic transition states which may permit the creation of excited-state species from less-exothermic reactions. Of course, since it is difficult to imagine a reaction which is endothermic in the ground state creating electronically excited species and since chemiluminescence is associated with heat release, it still seems reasonable to only permit reactions which are exothermic in the ground state to create excited-state species. Based on the results herein (which corroborate the existence of R2), the requirement that ΔH_R^0 for the ground-state reaction exceed ΔE could be relaxed so as to permit less-exothermic reactions to form excited-state species.

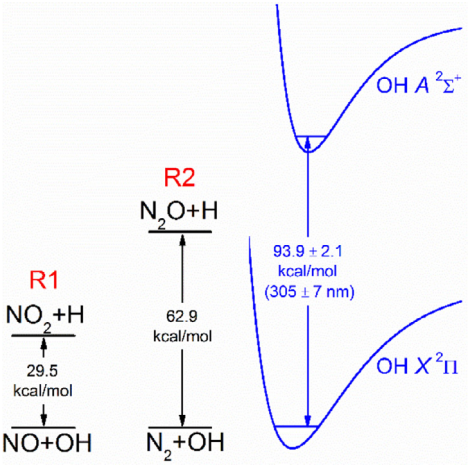

Fig. 14. Illustrations of ΔH_R^0 for the ground-state forms of R1 and R2 alongside an illustration of ΔE for the OH $A \rightarrow X$ transition (potential energy curves for OH not drawn to scale).

5.5. Identifying new chemiluminescent reactions

Lacking in the literature is a systematic framework for identifying new chemiluminescent reactions. To aid in the development of such a framework, an investigation of ΔH_R^0 and the standard-state entropy of reaction (ΔS_R^0) of several well-known chemiluminescent reactions for OH*, CH*, and CO_2* and their ground-state analogs was performed and is summarized in Table 2. Other than the reactions R1 and R2, the ground-state forms of the chemiluminescent reactions possess a ΔH_R^0 which surpasses ΔE in magnitude.

Table 2
Emitted λ, associated ΔE, ΔH_R^0, and ΔS_R^0 for chemiluminescent reactions involving OH*, CH*, and CO_2* as well as their ground-state analogs. Thermochemistry for OH* and CH* is from Burcat and Ruscic [51]; other thermochemistry is from Glarborg et al. [47]; see footnotes regarding CO_2*.

Reaction	λ (nm)	ΔE (kcal/mol)	ΔH_R^0 (kcal/mol)	ΔS_R^0 (cal/mol K)	ΔH_R^0, ground state (kcal/mol)	ΔS_R^0, ground state (cal/mol K)	Reference
$NO_2 + H \rightleftarrows NO + OH^*$	305	−93.9	64.4	8.4	−29.5	9.5	This study
$N_2O + H \rightleftarrows N_2 + OH^*$	305	−93.9	31.0	8.6	−62.9	9.7	[6]
$O + H (+M) \rightleftarrows OH^* (+M)$	305	−93.9	−8.8	−23.1	−102.7	−22.0	[34]
$CH + O_2 \rightleftarrows CO + OH^*$	305	−93.9	−66.0	−2.7	−159.9	−1.6	[49]
$C_2 + OH \rightleftarrows CO + CH^*$	427	−66.9	−23.9	−1.7	−91.0	−0.6	[52]
$C_2H + O \rightleftarrows CO + CH^*$	427	−66.9	−12.2	0.4	−79.3	1.5	[52]
$CO + O (+M) \rightleftarrows CO_2^* (+M)$	415[a]	−68.9	−58.3	−34.6[b]	−127.2	−34.6	[53]

[a] CO_2* exhibits a broadband emission from ~340 to ~650 nm. In the referenced work, both 415 and 458 nm were used to monitor CO_2*.
[b] S^0 for CO_2* was assumed to be equal to that of CO_2 as was assumed by Kopp et al. [53].

As for the ΔS_R^0 values in Table 2, no unmistakable trend can be observed; the values range from −34.6 to 9.7 cal/mol K with no obvious correlation to any other parameters in Table 2. However, a more-subtle trend may be present. It appears ground-state reactions for which ΔH_R^0 is larger in magnitude than ΔE can possess a chemiluminescent analog despite having a negative ΔS_R^0, while ground-state reactions for which ΔH_R^0 is smaller in magnitude than ΔE may still possess a chemiluminescent analog if ΔS_R^0 is positive. In light of these observations, the following set of criteria are tentatively proposed for identifying new chemiluminescent reactions:

I. Consider exothermic reactions that produce the ground-state form of the chemiluminescent species
II. Give preference to more-exothermic reactions for which the magnitude of ΔH_R^0 is larger than that of ΔE, regardless of the sign of ΔS_R^0
III. Give secondary preference to less-exothermic reactions for which the magnitude of ΔH_R^0 is smaller than that of ΔE if ΔS_R^0 is positive

The values of ΔH_R^0 and ΔS_R^0 in the criteria above refer to those of the ground-state reaction. An additional consideration is that neither the forward nor backward collisional limits of a proposed chemiluminescent rate coefficient should be exceeded; this is related to the concentrations of the reactants and products. Finally, reactions which produce the ground-state form of the chemiluminescent species and are known to be important for heat release may further suggest the existence of a chemiluminescent analog, although this is not always the case (Section 5.1).

One could imagine that the inadequacy of the ΔH_R^0 screening technique for identifying possible chemiluminescent reactions might be due to the fact that ΔH_R^0 is typically evaluated at room temperature rather than flame temperatures. Actually, ΔH_R^0 is generally a rather weak function of temperature. For example, evaluating ΔH_R^0 at 2000 K for the ground-state form of R1 using the thermochemistry of Glarborg et al. [47] yields −32.5 kcal/mol, which is within 10% of the value of −29.5 kcal/mol. Evaluating ΔS_R^0 at 2000 K for the ground-state form of R1 yields 6.8 cal/mol K, which is a ~30% reduction from the value of 9.5 cal/mol K.

6. Conclusions

OH* profiles were obtained behind reflected shock waves in a mixture of H_2–NO_2 for the first time. Using these unique data, the new OH*-forming reaction $NO_2 + H \leftrightarrows NO + OH^*$ (R1) was identified. The identification of R1 was based on the known importance of the ground-state analog to heat release in H_2–NO_2 mixtures, analogy to $N_2O + H \leftrightarrows N_2 + OH^*$ (R2), and detailed kinetic modeling efforts. OH* profiles were also obtained in a mixture of H_2–N_2O. The addition of R1 had no effect on the modeling of the newly obtained H_2–N_2O data, nor on previously obtained H_2–N_2O data from Hidaka et al. [6]. The addition of R1 also had no effect on the modeling of previously acquired OH* data in the NH_3–O_2 system (see the SM). The lack of effect of R1 in modeling these two fuel systems suggested the introduction of R1 should not degrade the predictions of other OH* data in the literature.

The best-fit k_1 was dependent on the choice of the base (i.e., ground-state) H_2–NOx mechanism, with the mechanism dependence arising from different predictions of H, O, and NO_2 concentrations. The best-fit k_1 using the mechanism of Glarborg et al. [47] was 5 times lower than the preferred value of k_1 obtained using the mechanism of Zhang et al. [32]. The best-fit k_1 remained below the forward and backward collision limits in the temperature range of the present study; the backward rate constant begins to exceed the backward collision limit near 750 K. The proposed expression for k_1 is valid in the temperature range of the present study (1535–2003 K).

The ground-state form of R1 is insufficiently exothermic to satisfy the oft-used criterion that ΔH_R^0 of the ground-state reaction be greater than the change in energy associated with the chemiluminescent emission. This finding, in conjunction with the similar findings of Hidaka et al. [6] regarding the endothermicity of R2, implies that this minimum-energy-release criterion can be relaxed in future searches for chemiluminescent reactions such that less-exothermic reactions can be considered as possible chemiluminescent reactions. Based on the considerations of the ground-state forms of R1 and R2 discussed herein, a better method of identifying reactions with a possible chemiluminescent analog is to consider the values of ΔS_R^0, ΔH_R^0, and ΔE for exothermic reactions that produce the ground-state forms of the excited-state species according to the criteria proposed in this paper.

Declaration of Competing Interest

The authors declare that they have no known competing financial interests or personal relationships that could have appeared to influence the work reported in this paper.

Acknowledgments

The authors wish to thank Prof. W.D. Kulatilaka for the use of the spectrometer. Funding for this work came from the National Science Foundation under award number CBET-1706825. The authors also acknowledge insightful comments from the reviewers pertaining to the identification of R1 and the importance of ΔS_R^0.

Supplementary materials

Supplementary material associated with this article can be found, in the online version, at doi:10.1016/j.combustflame.2019.11.010.

References

[1] W. Tsang, J.T. Herron, Chemical kinetic data base for propellant combustion I. Reactions involving NO, NO_2, HNO, HNO_2, HCN and N_2O, J. Phys. Chem. Ref. Data 20 (1991) 609–663.

[2] C.R. Mulvihill, O. Mathieu, E.L. Petersen, The unimportance of the reaction $H_2 + N_2O \leftrightarrows H_2O + N_2$: a shock-tube study using H_2O time histories and ignition delay times, Combust. Flame 196 (2018) 478–486.

[3] V. Sick, High speed imaging in fundamental and applied combustion research, Proc. Comb. Inst. 34 (2013) 3509–3530.

[4] R.I. Soloukhin, P.J. Van Tiggelen, Shock tube study of the induction lag in nitrous oxide-hydrogen system, Bulletin des Sociétés Chimiques Belges 78 (1969) 179–189.

[5] R.I. Soloukhin, High-temperature oxidation of hydrogen by nitrous oxide in shock waves, Symp. (Int.) Combust. 14 (1973) 77–82.

[6] Y. Hidaka, H. Takuma, M. Suga, Shock-tube study of the rate constant for excited OH^* ($^2\Sigma^+$) formation in the N_2O–H_2 reaction, J. Phys. Chem. 89 (1985) 4903–4905.

[7] R. Mével, F. Lafosse, L. Catoire, N. Chaumeix, G. Dupré, C.-.E. Paillard, Induction delay times and detonation cell size prediction of hydrogen-nitrous oxide-diluent mixtures, Comb. Sci. Tech. 180 (2008) 1858–1875.

[8] R. Mével, S. Javoy, F. Lafosse, N. Chaumeix, G. Dupré, C.-.E. Paillard, Hydrogen–nitrous oxide delay times: shock tube experimental study and kinetic modelling, Proc. Comb. Inst. 32 (2009) 359–366.

[9] R. Mével, S. Pichon, L. Catoire, N. Chaumeix, C.-.E. Paillard, J.E. Shepherd, Dynamics of excited hydroxyl radicals in hydrogen-based mixtures behind reflected shock waves, Proc. Comb. Inst. 34 (2013) 677–684.

[10] O. Mathieu, E.L. Petersen, Experimental and modeling study on the high-temperature oxidation of ammonia and related NOx chemistry, Combust. Flame 162 (2015) 554–570.

[11] A. Snyder, J. Robertson, D. Zanders, G. Skinner, Shock-tube studies of fuel-air ignition characteristics, Monsanto Research Corporation, 1965 Report No. AFAPL-TR-65-93.

[12] O. Mathieu, A. Levacque, E.L. Petersen, Effects of NO_2 addition on hydrogen ignition behind reflected shock waves, Proc. Comb. Inst. 34 (2013) 633–640.

[13] M.A. Mueller, R.A. Yetter, F.L. Dryer, Flow reactor studies and kinetic modeling of the $H_2/O_2/NO_x$ and $CO/H_2O/O_2/NO_x$ reactions, Int. J. Chem. Kin. 31 (1999) 705–724.

[14] G. Dayma, P. Dagaut, Effects of air contamination on the combustion of hydrogen—Effect of NO and NO_2 addition on hydrogen ignition and oxidation kinetics, Comb. Sci. Tech. 178 (2006) 1999–2024.

[15] P.G. Ashmore, B.P. Levitt, The thermal reaction between hydrogen and nitrogen dioxide. Part 2. Experimental work on the kinetics of the reaction, Trans. Faraday Soc. 52 (1956) 835–848.

[16] P.G. Ashmore, B.P. Levitt, The thermal reaction between hydrogen and nitrogen dioxide. Part 3. Further experimental work on the kinetics: reaction mechanism, Trans. Faraday Soc. 53 (1957) 945–954.

[17] P.G. Ashmore, B.P. Levitt, The thermal reaction between hydrogen and nitrogen dioxide. Part 4. Thermal ignitions of hydrogen and nitrogen dioxide, Trans. Faraday Soc. 54 (1958) 390–393.

[18] W.A. Rosser, H. Wise, Kinetics of reaction between hydrogen and nitrogen dioxide, J. Chem. Phys. 26 (1957) 571–576.

[19] R.F. Sawyer, I. Glassman, The reactions of hydrogen with nitrogen dioxide, oxygen, and mixtures of oxygen and nitric oxide, Symp. (Int.) Combust. 12 (1969) 469–479.

[20] J. Park, N.D. Giles, J. Moore, M.C. Lin, A comprehensive kinetic study of thermal reduction of NO_2 by H_2, J. Phys. Chem. A 102 (1998) 10099–10105.

[21] M.A. Mueller, J.L. Gatto, R.A. Yetter, F.L. Dryer, Hydrogen/nitrogen dioxide kinetics: derived rate data for the reaction $H_2 + NO_2 = HONO + H$ at 833 K, Combust. Flame 120 (2000) 589–594.

[22] F. Joubert, D. Desbordes, H.-.N. Presles, Detonation cellular structure in NO_2/N_2O_4-fuel gaseous mixtures, Combust. Flame 152 (2008) 482–495.

[23] F. Virot, B. Khasainov, D. Desbordes, H.-.N. Presles, Numerical simulation of the influence of tube diameter on detonation regime and structure in mixtures with two-step energy release and double cellular structure, Combust Explos Shock Waves 45 (2009) 435–441.

[24] F. Virot, B. Khasainov, D. Desbordes, H.N. Presles, Two-cell detonation: losses effects on cellular structure and propagation in rich H_2–NO_2/N_2O_4–Ar mixtures, Shock Waves 20 (2010) 457–465.

[25] D. Davidenko, R. Mével, G. Dupré, Numerical study of the detonation structure in rich H_2-NO_2/N_2O_4 and very lean H_2-N_2O mixtures, Shock Waves 21 (2011) 85–99.

[26] C.R. Mulvihill, O. Mathieu, E.L. Petersen, H_2O time histories in the H_2-NO_2 system for validation of NO_x hydrocarbon kinetics mechanisms, Int. J. Chem. Kin. 51 (2019) 669–678.

[27] W. Schneider, G.K. Moortgat, G.S. Tyndall, J.P. Burrows, Absorption cross-sections of NO_2 in the UV and visible region (200–700 nm) at 298 K, Journal of Photochem. Photobiol. A 40 (1987) 195–217.

[28] T.C. Hall, F.E. Blacet, Separation of the absorption spectra of NO_2 and N_2O_4 in the range of 2400–5000A, J. Chem. Phys. 20 (1952) 1745–1749.

[29] J.T.C. Liu, R.K. Hanson, J.B. Jeffries, High-sensitivity absorption diagnostic for NO_2 using a blue diode laser, J. Quant. Spec. Rad. Trans. 72 (2002) 655–664.

[30] B.P. Levitt, Thermal emission from nitrogen dioxide, Trans. Faraday Soc. 58 (1962) 1789–1800.

[31] D.E. Paulsen, W.F. Sheridan, R.E. Huffman, Thermal and recombination emission of NO_2, J. Chem. Phys. 53 (1970) 647–658.

[32] Y. Zhang, O. Mathieu, E.L. Petersen, G. Bourque, H.J. Curran, Assessing the predictions of a NO_x kinetic mechanism on recent hydrogen and syngas experimental data, Combust. Flame 182 (2017) 122–141.

[33] C.R. Mulvihill, O. Mathieu, E.L. Petersen, Corrigendum to "The unimportance of the reaction $H_2 + N_2O \leftrightarrows H_2O + N_2$: a shock-tube study using H_2O time histories and ignition delay times", Combust. Flame 196 (2018) 478–486 Combust. Flame 204 (2019) 430.

[34] T. Kathrotia, M. Fikri, M. Bozkurt, M. Hartmann, U. Riedel, C. Schulz, Study of the H+O+M reaction forming OH^*: kinetics of OH^* chemiluminescence in hydrogen combustion systems, Combust. Flame 157 (2010) 1261–1273.

[35] M. Tamura, P.A. Berg, J.E. Harrington, J. Luque, J.B. Jeffries, G.P. Smith, D.R. Crosley, Collisional quenching of CH(A), OH(A), and NO(A) in low pressure hydrocarbon flames, Combust. Flame 114 (1998) 502–514.

[36] W.L. Dimpfl, J.L. Kinsey, Radiative lifetimes of oh($a\ ^2\Sigma$) and Einstein coefficients for the a-x system of OH and OD, J. Quant. Spec. Rad. Trans. 21 (1979) 233–241.

[37] P.H. Paul, A model for temperature-dependent collisional quenching of OH $a\ ^2\Sigma^+$, J. Quant. Spec. Rad. Trans. 51 (1994) 511–524.

[38] P.H. Paul, J.L. Durant, J.A. Gray, M.R. Furlanetto, Collisional electronic quenching of OH $A^2\Sigma$ (v'=0) measured at high temperature in a shock tube, J. Chem. Phys. 102 (1995) 8378–8384.

[39] K.H. Becker, D. Haaks, T. Tatarczyk, The natural lifetime of OH ($^2\Sigma^+$, $v = 0$, $\underline{n} = 2$, $\underline{j} = 32$) and its quenching by atomic hydrogen, Chem. Phys. Let. 25 (1974) 564–567.

[40] P.W. Fairchild, G.P. Smith, D.R. Crosley, Collisional quenching of $A^2\Sigma^+$ OH at elevated temperatures, J. Chem. Phys. 79 (1983) 1795–1807.

[41] R.D. Kenner, F.P. Capetanakis, F. Stuhl, Kinetic isotope effects in the electronic quenching of OD/OH($a\ ^2\Sigma^+$,$v = 0$) at 296 ± 4 K, J. Phys. Chem. 94 (1990) 2441–2446.

[42] R.A. Copeland, M.J. Dyer, D.R. Crosley, Rotational-level-dependent quenching of $A^2\Sigma^+$ OH and OD, J. Chem. Phys. 82 (1985) 4022–4032.

[43] J.B. Jeffries, R.A. Copeland, D.R. Crosley, Quenching of OH($a\ ^2\Sigma^+$, $v' = 0$) by NH_3 from 250 to 1400 K, J. Chem. Phys. 85 (1986) 1898–1903.

[44] G. Blanchet, Digital Signal and Image Processing Using MATLAB, 1, Wiley, London, UK, 2014 Fundamentals.

[45] R. Mével, F. Lafosse, N. Chaumeix, G. Dupré, C.E. Paillard, Spherical expanding flames in H_2–N_2O–Ar mixtures: flame speed measurements and kinetic modeling, Int. J. Hydrogen Energy 34 (2009) 9007–9018.

[46] R.A. Svehla, Estimated viscosities and thermal conductivities of gases at high temperatures, NASA, 1962 Report No. TR R-132.

[47] P. Glarborg, J.A. Miller, B. Ruscic, S.J. Klippenstein, Modeling nitrogen chemistry in combustion, Prog. Ener. Comb. Sci. 67 (2018) 31–68.

[48] G. Yarwood, J.W. Sutherland, M.A. Wickramaaratchi, R.B. Klemm, Direct rate constant measurements for the reaction $O + NO + Ar \rightarrow NO_2 + Ar$ at 300–1341 K, J. Phys. Chem. 95 (1991) 8771–8775.

[49] J.M. Hall, E.L. Petersen, An optimized kinetics model for OH chemiluminescence at high temperatures and atmospheric pressures, Int. J. Chem. Kin. 38 (2006) 714–724.

[50] K.J. Laidler, K.E. Shuler, Elementary reactions in the gas phase involving excited electronic states, Chem. Rev. 48 (1951) 153–224.

[51] A. Burcat, B. Ruscic, Third millenium ideal gas and condensed phase thermochemical database for combustion, Argonne National Lab and Technion-Israel Institute of Technology, 2005 Report No. ANL-05/20 and TAE 960.

[52] V.N. Nori, J.M. Seitzman, CH^* chemiluminescence modeling for combustion diagnostics, Proc. Comb. Inst. 32 (2009) 895–903.

[53] M. Kopp, M. Brower, O. Mathieu, E. Petersen, F. Güthe, CO_2^* chemiluminescence study at low and elevated pressures, App. Phys. B 107 (2012) 529–538.